Astrodynamics Vol. 6, No. 4, 357–374, 2022 https://doi.org/10.1007/s42064-021-0110-4

Secular dynamics of navigation satellites in the MEO and GSO regions

Hanlun Lei[1,2](✉), **Emiliano Ortore**[3], **and Christian Circi**[3]

1. *School of Astronomy and Space Science, Nanjing University, Nanjing 210023, China*
2. *Key Laboratory of Modern Astronomy and Astrophysics in Ministry of Education, Nanjing University, Nanjing 210023, China*
3. *Department of Astronautical, Electrical and Energy Engineering, Sapienza University of Rome, Via Salaria 851, Rome 00138, Italy*

ABSTRACT

In this study, a dynamical model is developed to describe the secular evolution of navigation satellites under the geocentric reference frame with the Laplace orbit as the fundamental plane. The disturbing function, involving the effects of Earth's oblateness and lunisolar gravitational attraction, is averaged over the orbital periods of both the satellite and the perturbers. In the regions of medium-Earth orbits and geosynchronous orbits, there are varieties of lunisolar resonances for governing the secular dynamics of navigation satellites. Among these resonances, we are interested in the ones occurring at the critical inclinations as well as the lunar node resonances. For each resonance of interest, the resonant center and width are identified analytically. Finally, dynamical maps are compared with the analytical results.

KEYWORDS

secular resonances
Laplace plane
navigation satellites
dynamical maps

Research Article

Received: 10 June 2021
Accepted: 29 July 2021

1 Introduction

There are four global navigation satellite systems: the American Global Positioning System (GPS), Russian Global Navigation Satellite System (GLONASS), European Galileo System (GALILEO), and Chinese BeiDou constellations [1]. The navigation satellites in these constellations move in the regions of medium-Earth orbits (MEOs) and geosynchronous orbits (GSOs), which are filled with varieties of lunisolar resonances. As for navigation satellites, the dominant perturbation comes from the Earth's oblateness, which is the main cause of the precession of the nodal and apsidal lines, and the secondary perturbation arises from lunisolar gravitational attraction, which plays an important role in the long-term evolution of the eccentricity and inclination due to lunisolar resonances. Lunisolar resonances take place under the condition that the frequencies of satellite's nodal and apsidal precession as well as the regression rate of the lunar node satisfy $\dot{\varphi}_{k_1,k_2,k_3} = k_1\dot{\omega} + k_2\dot{\Omega} + k_3\dot{\Omega}_{\mathrm{M}} = 0$, where $k_1, k_2, k_3 \in \mathbb{Z}$, ω and Ω are the argument of pericenter and longitude of the ascending node of the satellite's orbit, respectively, and Ω_{M} is the longitude of the lunar node.

Concerning a distant Earth satellite, Allan and Cook obtained an analytical solution for the long-term variation of orbital plane under the approximation that the lunar orbit shares the same plane with the ecliptic, and they concluded that the orbital plane precesses around the Laplace plane periodically [2]. When the regression of the lunar node is considered, the dynamical model becomes non-autonomous, so that the orbital planes can no longer be frozen on the Laplace plane [3, 4]. Ulivieri *et al.* noticed lunar node resonances which happen between the satellite's node and the lunar node [4]. Zhu analytically studied the resonance condition, stability, and phase structures of the lunar node resonances and concluded that the orbital plane would exhibit long-term fluctuation due to nodal resonances [5].

In general, navigation satellites hold non-zero eccentricity and thus, in the long-term evolution, the eccentricity and inclination would exhibit coupled variations due to lunisolar resonances. In this context, Breite reviewed the lunisolar secular and semi-secular

✉ leihl@nju.edu.cn

resonances theoretically and classified them into several groups based on fundamental models [6]. To reveal the causes of orbital instability in the MEO region, Rosengren *et al.* investigated the main resonant structures in the phase space that govern the long-term orbital motion of navigation satellites [7]. Daquin *et al.* described the phase space as an exceedingly complicated web-like structure of lunisolar secular resonances, and they traced the topological organization of the manifolds on which chaotic motion occurs by analyzing the nature of the resonant interactions [8]. In particular, they introduced the fast Lyapunov indicator (FLI) and numerically calculated FLI stability maps to test the Chirikov criterion for resonance overlap. The FLI is a chaotic index which is usually used to distinguish stable, resonant, and chaotic orbits [9]. Gkolias *et al.* found that the FLI map depends on the initial longitude of the ascending node and the argument of pericenter [10]. Consequently, different FLI maps are produced when different initial values of the angles are used. To remove the angle dependence of conventional stability maps, they proposed angle-averaged FLI maps to characterize the degree of chaoticity. In dynamical maps, the structures arising in the action space are determined by the occurrence of lunisolar resonance [8, 10], and the structures arising in the angle space are related to the locations of the stable and unstable equilibria of the associated resonant model [11–13].

When the altitude of satellite is not low, the inclination of a circular or quasi-circular orbit exhibits long-period oscillation around the frozen solution (i.e., the Laplace plane). On the Laplace plane, the long-period perturbation due to the J_2 effect of the Earth counteracts the lunisolar long-period perturbations. Thus, it is possible to remove the long-period variation if the Laplace orbit is adopted as the reference plane of coordinate system (see Figs. 2 and 3). Naturally, the dependence of secular dynamics of navigation satellites upon the initial longitude of ascending node can be removed. In this study, we revisit the secular dynamics of navigation satellites moving in the MEO and GSO regions under the dynamical model formulated in the geocentric Laplace reference frame.

The remainder of this paper is organized as follows. In Section 2, the dynamical model is introduced. The lunisolar resonances are discussed in Section 3, and the determination of resonant width is described in Section 4. Dynamical maps are reported in Section 5, and the conclusions are presented in Section 6.

2 Dynamical model

Our previous paper presented explicit expressions of the double-averaged disturbing function under both the geocentric equatorial and ecliptic reference frames [14]. These two reference frames have a common x-axis direction, and the coordinates of satellites measured in both reference frames can be converted between each other using a rotation matrix along the x axis, $R_x(\pm\varepsilon)$, where $\varepsilon(=23.439°)$ is the obliquity of the ecliptic relative to the Earth's equator. Between the equatorial and ecliptic planes, there is an intermediate plane, called Laplace plane, which shares the same nodal line with the ecliptic [15]. Figure 1(a) shows the relative geometry of the Earth's equator, the ecliptic, and Laplace

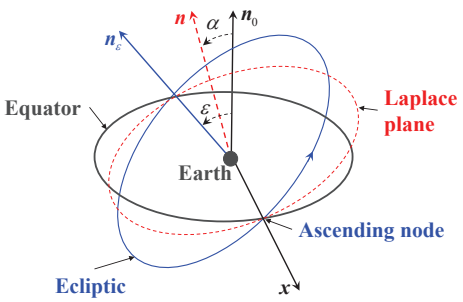

(a)

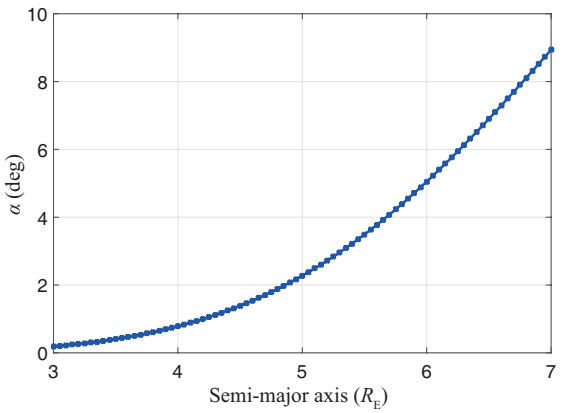

(b)

Fig. 1 Relative geometry of the Earth's equator, ecliptic, and Laplace planes (a) and the inclination of the Laplace plane relative to the Earth's equator as a function of the semimajor axis (b). The normal directions of the Earth's equator, the ecliptic, and Laplace plane are denoted by $\boldsymbol{n}_0$, $\boldsymbol{n}_\varepsilon$, and $\boldsymbol{n}$, respectively. The angular separation between $\boldsymbol{n}$ and $\boldsymbol{n}_0$ is denoted by α and the relative angle between $\boldsymbol{n}_\varepsilon$ and $\boldsymbol{n}_0$ is denoted by $\varepsilon(=23.439°)$.

orbit. By taking these orbits as the fundamental planes and their normal directions as the directions of the z axes, three right-handed reference frames with origins at the barycenter of the Earth can be defined and, for convenience, they are called the geocentric equatorial, ecliptic, and Laplace reference frames.

In a certain reference frame, the state of an object is described by orbital elements: the semimajor axis (a), eccentricity (e), inclination (i), longitude of the ascending node (Ω), argument of pericenter (ω), and mean anomaly (M). Alternatively, M can be replaced by the eccentric anomaly E or true anomaly f. For convenience, we use the variables with the subscripts S and M to represent the orbital elements of the Sun and the Moon, respectively, and the variables without subscripts to represent the orbital elements of navigation satellites. For the sake of computation accuracy, the variables are normalized by taking the mass of the Earth and the mean radius of Earth's equator as units of mass and length, respectively. The time unit is selected such that the universal gravitational constant $\mathcal{G}$ is equal to unity.

Unless otherwise specified, the orbits of the Sun and the Moon are described under the geocentric ecliptic reference frame, in which the inclination of the Sun is $i_{\rm S}=0^\circ$, the inclination of the lunar orbit is approximated as a constant ($i_{\rm S}\approx 5.09^\circ$), and both the longitude of the lunar ascending node and lunar argument of pericenter can be approximated as linear functions of time [16]. The nodal line of the lunar orbit regresses with a period of $\sim$18.61 years (i.e., $\dot{\Omega}_{\rm M}=-0.053$ deg/day), and the apsidal line precesses with a period of $\sim$8.85 years (i.e., $\dot{\omega}_{\rm M}=0.111$ deg/day) [7].

The Laplace plane is a stable equilibrium solution (or frozen solution) for satellites moving in circular orbits around the Earth (corresponding to the solution of $\dot{\Omega}=0$ and $\dot{i}=0$). By determining the frozen condition, the inclination of the Laplace plane relative to the equator, denoted by α, can be obtained as a function of the semimajor axis of the satellite in the following form (the eccentricities of satellites are assumed to be zero, and those terms involving the angle $\Omega_{\rm M}$, which is on the order of $\sin i_{\rm M}$, are neglected):

$$\tan 2\alpha=\frac{[2\mathcal{C}_2+(3\cos^2 i_{\rm M}-1)\mathcal{C}_3]\sin 2\varepsilon}{4\mathcal{C}_1+[2\mathcal{C}_2+(3\cos^2 i_{\rm M}-1)\mathcal{C}_3]\cos 2\varepsilon} \tag{1}$$

The coefficients in Eq. (1) are given by

$$\mathcal{C}_1=\frac{1}{2}\frac{J_2\mu_{\rm E}R_{\rm E}^2}{a^3}$$

$$\mathcal{C}_2=\frac{1}{2}\frac{\mu_{\rm S}}{a_{\rm S}}\left(\frac{a}{a_{\rm S}}\right)^2\frac{1}{(1-e_{\rm S}^2)^{3/2}}$$

$$\mathcal{C}_3=\frac{1}{2}\frac{\mu_{\rm M}}{a_{\rm M}}\left(\frac{a}{a_{\rm M}}\right)^2\frac{1}{(1-e_{\rm M}^2)^{3/2}}$$

where $\mu_{\rm E}=\mathcal{G}M_{\rm E}$ and $R_{\rm E}$ are the gravitational parameter and mean equatorial radius of the Earth, respectively, and a_{3b}, e_{3b}, i_{3b}, and $\mu_{3b}=\mathcal{G}M_{3b}$ are the semimajor axis, eccentricity, inclination, and gravitational parameter of the Sun or the Moon (in the entire work the subscript $3b$ represents S for the Sun or M for the Moon). In practical computations, we take the following parameters: $a_{\rm S}=1$ au, $a_{\rm M}=384{,}400$ km, $e_{\rm S}=0.0167$, $e_{\rm M}=0.0549$, $i_{\rm S}=0^\circ$, and $i_{\rm M}=5.09^\circ$. It is not difficult to show that, when the lunar inclination relative to the ecliptic is set as zero (i.e., $i_{\rm M}=0^\circ$), Eq. (1) can be reduced to the conventional expression [2, 4]:

$$\tan 2\alpha=\frac{(\mathcal{C}_2+\mathcal{C}_3)\sin 2\varepsilon}{2\mathcal{C}_1+(\mathcal{C}_2+\mathcal{C}_3)\cos 2\varepsilon}$$

In Fig. 1(b), the inclination of the Laplace plane relative to the equator is plotted as a function of the semimajor axis. Clearly, α increases with the semimajor axis, showing that the difference between the geocentric equatorial and Laplace reference frames can be neglected for satellites moving in low Earth orbit but it is significant for high-altitude satellites.

On the Laplace plane, the long-period perturbations resulting from the J_2 effect and lunisolar gravitation cancel each other out for circular or nearly circular orbits. If the Laplace orbit is taken as the reference plane to measure satellite orbits, the evolution of the inclination depends weakly on the longitude of the ascending node, indicating that the long-period oscillations of the satellite's inclination can be greatly reduced. To show this behavior, a practical trajectory measured in three different reference frames is presented in Fig. 2, which shows that, in the geocentric Laplace frame, the evolution of the inclination is relatively stable, and the longitude of the ascending node exhibits quasi-linear evolution with respect to time. However, in the geocentric equatorial or ecliptic reference frame, the inclination shows a periodic variation with large magnitude, and the longitude of the ascending node changes nonlinearly with time.

As discussed in Ref. [14], it is expected to find a reference frame in which the longitude of the ascending

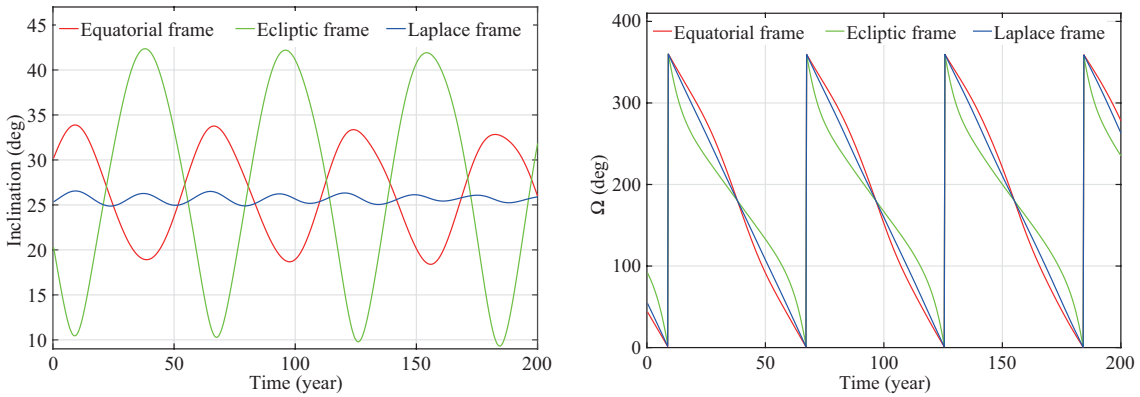

(a) (b)

Fig. 2 Time histories of the inclination (a) and longitude of the ascending node (b) measured in three different reference frames for the trajectory with initial elements of $a_0 = 6.61R_{\mathrm{E}}$ and $e_0 = 0.001$.

node undergoes quasi-linear evolution in order to study secular resonances in low-eccentricity regions. Thus, the geocentric Laplace reference frame is a good choice. In the following, we adopt the geocentric Laplace reference frame to formulate the dynamical model of navigation satellites and revisit the dynamics of secular resonances.

In the studies of long-term dynamics, the disturbing function is averaged over the orbital periods of the satellite and the perturbing body. Following the procedure described in Refs. [14, 17], we take into account the leading terms of the perturbation due to the Earth's oblateness and of the lunisolar gravitational perturbations to derive an explicit expression for the double-averaged disturbing function under the geocentric Laplace reference frame as Eq. (2):

$$
\begin{aligned}
\langle\langle\mathcal{R}\rangle\rangle = {} & \frac{1}{2}\frac{\mu_{\mathrm{E}}R_{\mathrm{E}}^2J_2}{a^3(1-e^2)^{3/2}}\left[\frac{1}{8}(3\cos 2\alpha+1)(3\cos^2 i-1)\right.\\
& \left.-\frac{3}{4}\sin 2\alpha\sin 2i\cos\Omega+\frac{3}{4}\sin^2\alpha\sin^2 i\cos 2\Omega\right]\\
& +\sum_{3b\in\{\mathrm{S,M}\}}\frac{1}{2}\frac{\mu_{3b}}{a_{3b}}\left(\frac{a}{a_{3b}}\right)^2\frac{1}{(1-e_{3b}^2)^{3/2}}\\
& \times\left[+\frac{1}{32}(3e^2+2)(3\cos^2(\varepsilon-\alpha)-1)(3\cos^2 i_{3b}-1)\right.\\
& \cdot(3\cos^2 i-1)\\
& +\frac{15}{128}e^2(1-\cos(\varepsilon-\alpha))^2\sin^2 i_{3b}(1+\cos i)^2\\
& \cdot\cos(2\Omega+2\omega+2\Omega_{3b})\\
& -\frac{15}{64}e^2\sin(\varepsilon-\alpha)(1-\cos(\varepsilon-\alpha))\sin 2i_{3b}(1+\cos i)^2\\
& \cdot\cos(2\Omega+2\omega+\Omega_{3b})\\
& +\frac{15}{64}e^2\sin^2(\varepsilon-\alpha)(3\cos^2 i_{3b}-1)(1+\cos i)^2\\
& \cdot\cos(2\Omega+2\omega)\\
& +\frac{15}{64}e^2\sin(\varepsilon-\alpha)(1+\cos(\varepsilon-\alpha))\sin 2i_{3b}(1+\cos i)^2\\
& \cdot\cos(2\Omega+2\omega-\Omega_{3b})\\
& +\frac{15}{128}e^2(1+\cos(\varepsilon-\alpha))^2\sin^2 i_{3b}(1+\cos i)^2\\
& \cdot\cos(2\Omega+2\omega-2\Omega_{3b})\\
& -\frac{15}{32}e^2\sin(\varepsilon-\alpha)(1-\cos(\varepsilon-\alpha))\sin^2 i_{3b}\sin i(1+\cos i)\\
& \cdot\cos(\Omega+2\omega+2\Omega_{3b})\\
& +\frac{15}{32}e^2(1-\cos(\varepsilon-\alpha))(1+2\cos(\varepsilon-\alpha))\sin 2i_{3b}\\
& \cdot\sin i(1+\cos i)\cos(\Omega+2\omega+\Omega_{3b})\\
& -\frac{15}{32}e^2\sin 2(\varepsilon-\alpha)(3\cos^2 i_{3b}-1)\sin i(1+\cos i)\\
& \cdot\cos(\Omega+2\omega)\\
& +\frac{15}{32}e^2(1-2\cos(\varepsilon-\alpha))(1+\cos(\varepsilon-\alpha))\sin 2i_{3b}\\
& \cdot\sin i(1+\cos i)\cos(\Omega+2\omega-\Omega_{3b})\\
& +\frac{15}{32}e^2\sin(\varepsilon-\alpha)(1+\cos(\varepsilon-\alpha))\sin^2 i_{3b}\sin i(1+\cos i)\\
& \cdot\cos(\Omega+2\omega-2\Omega_{3b})\\
& +\frac{45}{64}e^2\sin^2(\varepsilon-\alpha)\sin^2 i_{3b}\sin^2 i\cos(2\omega+2\Omega_{3b})\\
& -\frac{45}{64}e^2\sin 2(\varepsilon-\alpha)\sin 2i_{3b}\sin^2 i\cos(2\omega+\Omega_{3b})\\
& +\frac{15}{32}e^2(3\cos^2(\varepsilon-\alpha)-1)(3\cos^2 i_{3b}-1)\sin^2 i\cos(2\omega)\\
& -\frac{45}{64}e^2\sin 2(\varepsilon-\alpha)\sin 2i_{3b}\sin^2 i\cos(2\omega-\Omega_{3b})\\
& +\frac{45}{64}e^2\sin^2(\varepsilon-\alpha)\sin^2 i_{3b}\sin^2 i\cos(2\omega-2\Omega_{3b})
\end{aligned}
$$

$$
\begin{aligned}
&+\frac{15}{128}e^2(1-\cos(\varepsilon-\alpha))^2\sin^2 i_{3b}(1-\cos i)^2\\
&\cdot\cos(2\Omega-2\omega+2\Omega_{3b})\\
&-\frac{15}{64}e^2\sin(\varepsilon-\alpha)(1-\cos(\varepsilon-\alpha))\sin 2i_{3b}(1-\cos i)^2\\
&\cdot\cos(2\Omega-2\omega+\Omega_{3b})\\
&+\frac{15}{64}e^2\sin^2(\varepsilon-\alpha)(3\cos^2 i_{3b}-1)(1-\cos i)^2\\
&\cdot\cos(2\Omega-2\omega)\\
&+\frac{15}{64}e^2\sin(\varepsilon-\alpha)(1+\cos(\varepsilon-\alpha))\sin 2i_{3b}(1-\cos i)^2\\
&\cdot\cos(2\Omega-2\omega-\Omega_{3b})\\
&+\frac{15}{128}e^2(1+\cos(\varepsilon-\alpha))^2\sin^2 i_{3b}(1-\cos i)^2\\
&\cdot\cos(2\Omega-2\omega-2\Omega_{3b})\\
&+\frac{15}{32}e^2\sin(\varepsilon-\alpha)(1-\cos(\varepsilon-\alpha))\sin^2 i_{3b}\sin i(1-\cos i)\\
&\cdot\cos(\Omega-2\omega+2\Omega_{3b})\\
&+\frac{15}{32}e^2(2\cos(\varepsilon-\alpha)+1)(\cos(\varepsilon-\alpha)-1)\sin 2i_{3b}\\
&\cdot\sin i(1-\cos i)\cos(\Omega-2\omega+\Omega_{3b})\\
&+\frac{15}{32}e^2\sin 2(\varepsilon-\alpha)(3\cos^2 i_{3b}-1)\sin i(1-\cos i)\\
&\cdot\cos(\Omega-2\omega)\\
&+\frac{15}{32}e^2(1+\cos(\varepsilon-\alpha))(2\cos(\varepsilon-\alpha)-1)\sin 2i_{3b}\\
&\cdot\sin i(1-\cos i)\cos(\Omega-2\omega-\Omega_{3b})\\
&-\frac{15}{32}e^2\sin(\varepsilon-\alpha)(1+\cos(\varepsilon-\alpha))\sin^2 i_{3b}\sin i(1-\cos i)\\
&\cdot\cos(\Omega-2\omega-2\Omega_{3b})\\
&+\frac{3}{64}(3e^2+2)(1-\cos(\varepsilon-\alpha))^2\sin^2 i_{3b}\sin^2 i\\
&\cdot\cos(2\Omega+2\Omega_{3b})\\
&-\frac{3}{32}(3e^2+2)\sin(\varepsilon-\alpha)(1-\cos(\varepsilon-\alpha))\sin 2i_{3b}\sin^2 i\\
&\cdot\cos(2\Omega+\Omega_{3b})\\
&+\frac{3}{32}(3e^2+2)\sin^2(\varepsilon-\alpha)(3\cos^2 i_{3b}-1)\sin^2 i\cos(2\Omega)\\
&+\frac{3}{32}(3e^2+2)\sin(\varepsilon-\alpha)(1+\cos(\varepsilon-\alpha))\sin 2i_{3b}\sin^2 i\\
&\cdot\cos(2\Omega-\Omega_{3b})\\
&+\frac{3}{64}(3e^2+2)(1+\cos(\varepsilon-\alpha))^2\sin^2 i_{3b}\sin^2 i\\
&\cdot\cos(2\Omega-2\Omega_{3b})\\
&+\frac{3}{32}(3e^2+2)\sin(\varepsilon-\alpha)(1-\cos(\varepsilon-\alpha))\sin^2 i_{3b}\sin 2i\\
&\cdot\cos(\Omega+2\Omega_{3b})\\
&+\frac{3}{32}(3e^2+2)(2\cos(\varepsilon-\alpha)+1)(\cos(\varepsilon-\alpha)-1)\sin 2i_{3b}\\
&\cdot\sin 2i\cos(\Omega+\Omega_{3b})\\
&+\frac{3}{32}(3e^2+2)\sin 2(\varepsilon-\alpha)(3\cos^2 i_{3b}-1)\sin 2i\cos\Omega\\
&+\frac{3}{32}(3e^2+2)(2\cos(\varepsilon-\alpha)-1)(\cos(\varepsilon-\alpha)+1)\sin 2i_{3b}\\
&\cdot\sin 2i\cos(\Omega-\Omega_{3b})\\
&-\frac{3}{32}(3e^2+2)\sin(\varepsilon-\alpha)(1+\cos(\varepsilon-\alpha))\sin^2 i_{3b}\sin 2i\\
&\cdot\cos(\Omega-2\Omega_{3b})\\
&+\frac{3}{32}(3e^2+2)\sin^2(\varepsilon-\alpha)\sin^2 i_{3b}(3\cos^2 i-1)\cos(2\Omega_{3b})\\
&-\frac{3}{32}(3e^2+2)\sin 2(\varepsilon-\alpha)\sin 2i_{3b}(3\cos^2 i-1)\cos\Omega_{3b}\Big]
\end{aligned}
\tag{2}
$$

where the elements (a,e,i,Ω,ω) are measured under the geocentric Laplace reference frame, and J_2 is the coefficient of the second-order zonal harmonics of the Earth (in practical computations, it is taken as 1.083×10^{-3}). The coefficients of the terms involving the angle $\pm2\omega$ are on the order of e^2, and thus these terms can be ignored if the eccentricity remains sufficiently small. In this case, the degrees of freedom are reduced by one, and the resulting simplified model is generally used to study the long-term evolution of satellites' orbital planes. In addition, the coefficients of the terms involving the angle $\pm2\Omega_{3b}$ contain the factor of $\sin^2 i_{3b}$, and the coefficients of the terms involving the angle $\pm\Omega_{3b}$ contain the factor of $\sin 2i_{3b}$. Thus, all the terms involving $\pm2\Omega_{\mathrm{S}}$ or $\pm\Omega_{\mathrm{S}}$ disappear from the disturbing function for the solar perturbation because of $i_{\mathrm{S}}=0°$.

In particular, there are two reduced cases for the disturbing function: (i) when the angle α is artificially assumed to be zero (i.e., the reference plane coincides with the Earth's equator), the double-averaged disturbing function represented by Eq. (2) naturally reduces to the form obtained under the geocentric equatorial reference frame [14], and (ii) when the angle α is artificially taken as ε (i.e., the reference frame coincides with the ecliptic), the double-averaged disturbing function represented by Eq. (2) reduces to the expression derived under the geocentric ecliptic reference frame [14]. Thus, we can easily retrieve the double-averaged disturbing function formulated under the geocentric Laplace, equatorial, or ecliptic reference frame by taking a certain value of α.

According to the expression shown in Eq. (2), the double-averaged disturbing function can be divided into secular terms (which are independent of the angular variables) and periodic terms (which are related to the

angular variables). Denote the periodic part by $\mathcal{R}_\mathrm{p}$. Figure 3 presents the variations of $\mathcal{R}_\mathrm{p}$ evaluated in the Laplace, equatorial, and ecliptic reference frames. For the same setting of parameters, the periodic part of the disturbing function measured in the geocentric Laplace reference frame is suppressed in a small range, which is expected from the viewpoint of perturbation treatment (the first-order perturbation theory is adopted in Section 3 to formulate the resonant models).

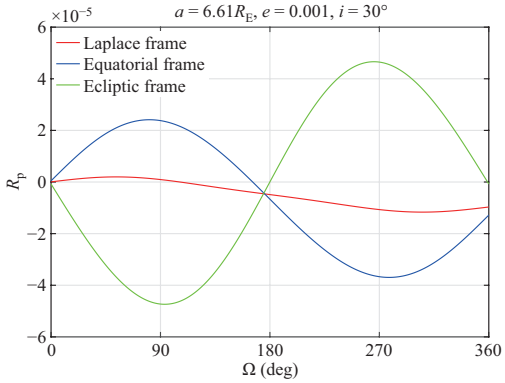

(a)

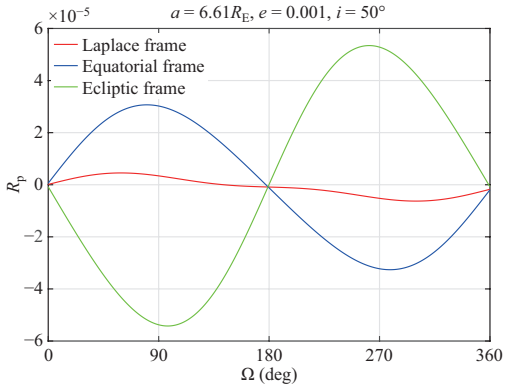

(b)

Fig. 3 Periodic terms of the double-averaged disturbing function.

The Delaunay action-angle variables,

$$\begin{cases} L = \sqrt{\mu_\mathrm{E} a}, & l = M \\ G = L\sqrt{1-e^2}, & g = \omega \\ H = G\cos i, & h = \Omega \end{cases} \tag{3}$$

are adopted to describe the dynamics of navigation satellites. Because the angle l is absent from the averaged dynamical model, its conjugated action L remains constant; that is, the semimajor axis remains stationary. In addition, the longitude of the lunar ascending node Ω_M depends explicitly on time, and thus the dynamical model is a non-autonomous system. To obtain an autonomous dynamical model, it is necessary to introduce an additional pair of conjugate variables:

$$T,\ \tau = \Omega_\mathrm{M} \tag{4}$$

where T is conjugate to τ (T is a constant). Consequently, the Hamiltonian of the system can be written as

$$\mathcal{H} = -\frac{\mu_\mathrm{E}^2}{2L^2} + \dot{\tau} \times T - \langle\langle \mathcal{R} \rangle\rangle \tag{5}$$

which describes a dynamical model with two and a half degrees of freedom. The equations of secular motion can be obtained by substituting the Hamiltonian given by Eq. (5) into the following canonical equations:

$$\begin{cases} \dot{g} = \dfrac{\partial \mathcal{H}}{\partial G},\ \dot{G} = -\dfrac{\partial \mathcal{H}}{\partial g} \\ \dot{h} = \dfrac{\partial \mathcal{H}}{\partial H},\ \dot{H} = -\dfrac{\partial \mathcal{H}}{\partial h} \\ \dot{\tau} = \dfrac{\partial \mathcal{H}}{\partial T},\ \dot{T} = -\dfrac{\partial \mathcal{H}}{\partial \tau} \end{cases} \tag{6}$$

In Section 5, the equation of motion given by Eq. (6) is used to produce dynamical maps.

3 Secular resonances

In the previous section, we formulated a dynamical model that describes the secular behavior of navigation satellites in the geocentric Laplace reference frame. In this section, we study the secular resonances using the formulated Hamiltonian model.

3.1 Resonance curves

The averaged Hamiltonian is composed of secular and periodic parts. The terms that are independent of the angle variables (h, g, and τ) belong to the secular part, and the remaining terms belong to the periodic part. The critical arguments appearing in the periodic part are denoted by

$$\varphi_{k_1,k_2,k_3} = k_1 h + k_2 g + k_3 \tau = k_1 \Omega + k_2 \omega + k_3 \Omega_\mathrm{M} \tag{7}$$

where k_1 is in $\{0,1,2\}$, k_2 is in $\{-2,0,2\}$, and k_3 is in $\{-2,-1,0,1,2\}$. When the time rate of φ_{k_1,k_2,k_3} is zero, secular resonance occurs. The effect of secular resonance on the dynamics depends on the expression of the critical argument. In particular, resonances with critical arguments in the form of $\varphi_{k_1,0,k_3}$, which are called nodal resonances, affect only the evolution of the inclination (i.e., they change the normal direction of the orbital plane), and other resonances have dynamical effects on both the eccentricity and inclination (i.e., they

change the normal direction and shape of the orbital plane simultaneously).

The resonance condition is given by

$$\dot{\varphi}_{k_1,k_2,k_3} = k_1\dot{h} + k_2\dot{g} + k_3\dot{\tau} = k_1\dot{\Omega} + k_2\dot{\omega} + k_3\dot{\Omega}_{\mathrm{M}} = 0 \tag{8}$$

where the precession rate of the apsidal line and the regression rate of the nodal line can be approximated by substituting the secular part of the disturbing function given by Eq. (2) into the Lagrange planetary equations:

$$\begin{aligned}
\dot{\Omega} =& -\frac{3}{4}J_2 n\left(\frac{R_{\mathrm{E}}}{a}\right)^2(3\cos^2\alpha-1)\frac{\cos i}{(1-e^2)^2} \\
&-\sum_{3b\in\{\mathrm{S,M}\}}\frac{3}{32}(3e^2+2)(3\cos^2(\varepsilon-\alpha)-1) \\
&\cdot\frac{\mu_{3b}(3\cos^2 i_{3b}-1)}{a_{3b}^3(1-e_{3b}^2)^{3/2}}\frac{\cos i}{n\sqrt{1-e^2}} \\
\dot{\omega} =& \frac{3}{8}J_2 n\left(\frac{R_{\mathrm{E}}}{a}\right)^2(3\cos^2\alpha-1)\frac{5\cos^2 i-1}{(1-e^2)^2} \\
&+\sum_{3b\in\{\mathrm{S,M}\}}\frac{1}{64}(3\cos^2(\varepsilon-\alpha)-1) \\
&\cdot\frac{\mu_{3b}(3\cos^2 i_{3b}-1)}{a_{3b}^3(1-e_{3b}^2)^{3/2}}\frac{30\cos^2 i+6(e^2-1)}{n\sqrt{1-e^2}}
\end{aligned} \tag{9}$$

where n is the mean motion of the satellite and is given by $n^2a^3 = \mu_{\mathrm{E}}$. By solving the resonance equation given by Eq. (8), the solution can be expanded to a series of three dimensional (3D) surfaces in the space (a, e, i) to reveal the distribution of the resonance locations. One secular resonance corresponds to one or two 3D surfaces. When one of the parameters a, e, or i is fixed, the 3D surface reduces to a curve, which is called the resonance curve. In particular, the nodal resonance of $\varphi_{1,0,0} = \Omega$ occurs on the polar orbit; in addition, the resonances of $\varphi_{k_1,k_2\neq 0,0}$ make the dominant contributions to the secular evolution of the eccentricity and inclination, and their resonance locations appear at the critical inclinations, that is, $\sim 46.4°$ for $2\omega+2\Omega$, $\sim 56.1°$ for $2\omega+\Omega$, $\sim 63.4°$ for 2ω, $\sim 69.0°$ for $2\omega-\Omega$, and $\sim 73.2°$ for $2\omega-2\Omega$ [13, 18–20].

Figure 4 shows the distribution of the resonance curves in the space (e, i) for MEO satellites with the semimajor axis at $4.38R_{\mathrm{E}}$ and GSO satellites with the semimajor axis at $6.61R_{\mathrm{E}}$. Figure 5 presents the resonance curves in the space (a, i) when the eccentricities are fixed at $e = 0.01$ and $e = 0.2$.

Figures 4 and 5 show that (i) all the resonance curves form a complex network in phase space; (ii) the resonance

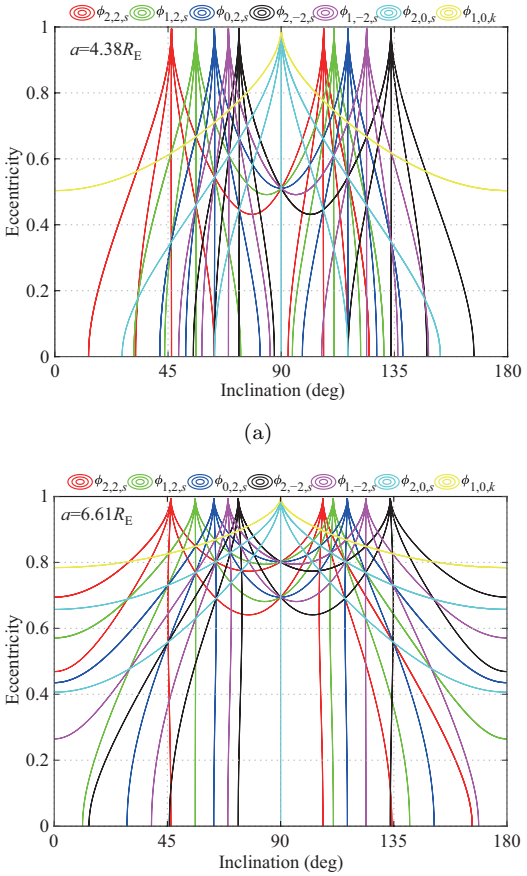

Fig. 4 Resonance curves in the space (e, i) for MEO satellites with semimajor axis of $a = 4.38R_{\mathrm{E}}$ (a) and GSO satellites with semimajor axis of $a = 6.61R_{\mathrm{E}}$ (b). The subscript s is in $\{2, 1, 0, -1, -2\}$, and k is in $\{2, -2\}$. The orbital elements are measured in the geocentric Laplace reference frame.

curves are symmetric with respect to the polar line; (iii) in the space (e, i), there are seven families of resonance curves, which are shown in different colors; and (iv) in both the spaces (e, i) and (a, i), the curves associated with the resonances of $\varphi_{k_1,k_2,0}$ are nearly vertical lines, which indicates that the locations of these resonances depend mainly on the inclination (they are known to occur at the critical inclinations). Note that, using the lunisolar disturbing function originally provided by Ref. [16], Ely and Howell [21] and Rosengren *et al.* [7] retrieved the resonance curves in the geocentric equatorial reference frame but they neglected the contribution of lunisolar perturbations when they computed the rates of nodal regression $\dot{\Omega}$ and apsidal precession $\dot{\omega}$.

3.2 Resonant Hamiltonian

To study the secular resonances, we need to formulate

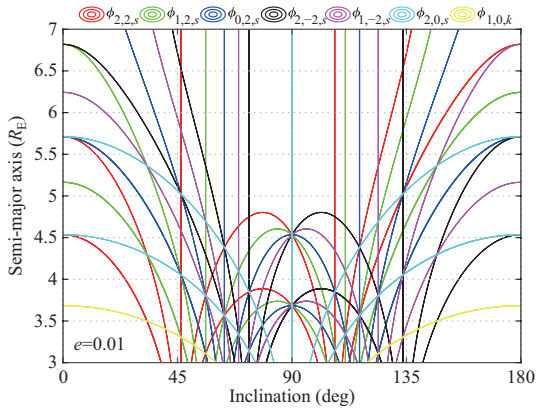

(a)

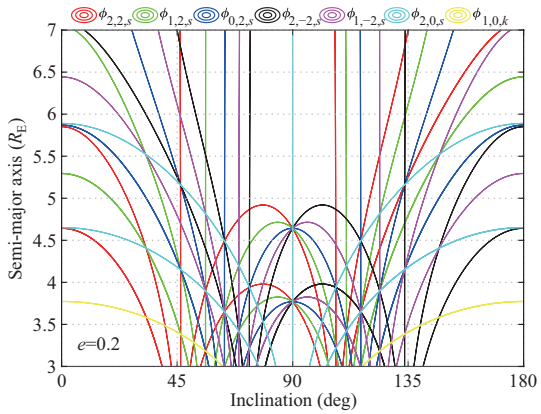

(b)

Fig. 5 Resonance curves distributed in the space (a, i) for eccentricity $e = 0.01$ (a) and $e = 0.2$ (b). The subscript s is in $\{2, 1, 0, -1, -2\}$, and k is in $\{2, -2\}$. The orbital elements are measured in the geocentric Laplace reference frame.

the resonant Hamiltonian. In the Hamiltonian function, the terms in the secular part are independent of the angle variables and can be written as Eq. (10):

$$\mathcal{H}_{\text{sec}} = -\frac{\mu_{\text{E}}^2}{2L^2} + \dot{\tau} \times T - \frac{1}{16}\mathcal{C}_{J_2}(3\cos 2\alpha + 1) \cdot \frac{1}{G^5}(3H^2 - G^2) - \frac{1}{32}\mathcal{C}_{\text{SM}}(3\cos^2(\varepsilon - \alpha) - 1) \cdot \frac{1}{G^2}(5L^2 - 3G^2)(3H^2 - G^2) \tag{10}$$

where the coefficients are

$$\mathcal{C}_{J_2} = \frac{J_2 R_{\text{E}}^2 \mu_{\text{E}}^4}{L^3},\ \mathcal{C}_{\text{SM}} = \mathcal{C}_{\text{S}} + \frac{1}{2}\mathcal{C}_{\text{M}}(3\cos^2 i_{\text{M}} - 1)$$

with

$$\mathcal{C}_{\text{S}} = \frac{\mu_{\text{S}}}{a_{\text{S}}^3}\frac{1}{(1 - e_{\text{S}}^2)^{3/2}}\frac{L^2}{\mu_{\text{E}}^2},\ \mathcal{C}_{\text{M}} = \frac{\mu_{\text{M}}}{a_{\text{M}}^3}\frac{1}{(1 - e_{\text{M}}^2)^{3/2}}\frac{L^2}{\mu_{\text{E}}^2}$$

The resonant terms in the Hamiltonian function that represent the secular resonances associated with critical arguments $\theta_1 = 2g+2h$, $\theta_2 = 2g+h$, $\theta_3 = 2g$, $\theta_4 = 2g-h$, and $\theta_5 = 2g - 2h$ are

$$\mathcal{H}_1 = -\frac{15}{64}\mathcal{C}_{\text{SM}}\sin^2(\varepsilon - \alpha)\frac{1}{G^2}(L^2 - G^2)(G + H)^2\cos\theta_1 \tag{11}$$

$$\mathcal{H}_2 = \frac{15}{32}\mathcal{C}_{\text{SM}}\sin 2(\varepsilon - \alpha)\frac{1}{G^2}(L^2 - G^2)(G + H) \cdot \sqrt{G^2 - H^2}\cos\theta_2 \tag{12}$$

$$\mathcal{H}_3 = -\frac{15}{32}\mathcal{C}_{\text{SM}}(3\cos^2(\varepsilon - \alpha) - 1)\frac{1}{G^2}(L^2 - G^2) \cdot (G^2 - H^2)\cos\theta_3 \tag{13}$$

$$\mathcal{H}_4 = -\frac{15}{32}\mathcal{C}_{\text{SM}}\sin 2(\varepsilon - \alpha)\frac{1}{G^2}(L^2 - G^2)(G - H) \cdot \sqrt{G^2 - H^2}\cos\theta_4 \tag{14}$$

and

$$\mathcal{H}_5 = -\frac{15}{64}\mathcal{C}_{\text{SM}}\sin^2(\varepsilon - \alpha)\frac{1}{G^2}(L^2 - G^2)(G - H)^2\cos\theta_5 \tag{15}$$

The resonant terms in the Hamiltonian that represent the lunar node resonances with critical arguments $\theta_6 = 2h - \tau$ and $\theta_7 = h - \tau$ are given by

$$\mathcal{H}_6 = -\frac{3}{64}\mathcal{C}_{\text{M}}\sin(\varepsilon - \alpha)(1 + \cos(\varepsilon - \alpha))\sin 2i_{\text{M}} \cdot \left(5\frac{L^2}{G^2} - 3\right)(G^2 - H^2)\cos\theta_6 \tag{16}$$

and

$$\mathcal{H}_7 = -\frac{3}{32}\mathcal{C}_{\text{M}}(2\cos(\varepsilon - \alpha) - 1)(\cos(\varepsilon - \alpha) + 1)\sin 2i_{\text{M}} \cdot \left(5\frac{L^2}{G^2} - 3\right)H\sqrt{G^2 - H^2}\cos\theta_7 - \frac{3}{128}\mathcal{C}_{\text{M}}(1 + \cos(\varepsilon - \alpha))^2\sin^2 i_{\text{M}}\left(5\frac{L^2}{G^2} - 3\right) \cdot (G^2 - H^2)\cos(2\theta_7) \tag{17}$$

When the satellite is locked inside a certain resonance, the corresponding resonant term in the Hamiltonian function becomes secular, and the remaining periodic terms are called nonresonant terms. The nonresonant terms can be removed from the Hamiltonian using the von Zeipel method [22, 23] or the Hori–Deprit method [24, 25]. To formulate the resonant model, we retain only the secular and resonant terms in the Hamiltonian function as follows: $\mathcal{H}_j^* = \mathcal{H}_{\text{sec}} + \mathcal{H}_j, j = 1, 2, 3, \cdots, 7$.

Consequently, the resonant model becomes a single-degree-of-freedom integrable system.

3.3 Secular resonances occurring at the critical inclinations

Five secular resonances occur at the critical inclinations, and their critical arguments are denoted by $\sigma = 2g + 2h$,

$\sigma = 2g + h$, $\sigma = 2g$, $\sigma = 2g - h$, and $\sigma = 2g - 2h$. The method used in this section is similar to that shown in Ref. [8].

3.3.1 $2g + 2h$ resonance

To study the secular resonance with critical argument $\sigma = 2g + 2h(= 2\omega + 2\Omega)$, we introduce a new set of conjugate variables $(\Sigma_1, \Sigma_2, \Sigma_3, \sigma_1, \sigma_2, \sigma_3)$, which are defined as

$$\begin{cases} \Sigma_1 = G - H, & \sigma_1 = g \\ \Sigma_2 = \frac{1}{2}H, & \sigma_2 = 2g + 2h = \sigma \\ \Sigma_3 = 2T, & \sigma_3 = \frac{1}{2}\tau \end{cases} \tag{18}$$

which is a canonical transformation with the generating function $\mathcal{S} = g(\Sigma_1 + 2\Sigma_2) + 2h\Sigma_2 + \frac{1}{2}\tau\Sigma_3$.

Consequently, the resonant Hamiltonian can be written as

$$\begin{aligned} \mathcal{H} = & -\frac{1}{16}\mathcal{C}_{J_2}(3\cos 2\alpha + 1)\left[\frac{12\Sigma_2^2}{(\Sigma_1+2\Sigma_2)^5} - \frac{1}{(\Sigma_1+2\Sigma_2)^3}\right] \\ & -\frac{1}{32}\mathcal{C}_{\mathrm{SM}}(3\cos^2(\varepsilon-\alpha) - 1)\left[\frac{5L^2}{(\Sigma_1+2\Sigma_2)^2} - 3\right] \\ & \cdot [12\Sigma_2^2 - (\Sigma_1+2\Sigma_2)^2] \\ & -\frac{15}{64}\mathcal{C}_{\mathrm{SM}}\sin^2(\varepsilon-\alpha)\left[L^2\frac{1}{(\Sigma_1+2\Sigma_2)^2} - 1\right] \\ & \cdot (\Sigma_1 + 4\Sigma_2)^2\cos\sigma_2 \end{aligned} \tag{19}$$

In the resonant model governed by Eq. (19), the angular coordinates σ_1 and σ_3 are cyclic, and thus their conjugate momenta Σ_1 and Σ_3 become the motion integral. This resonant model has one degree of freedom and is a totally integrable system with $\sigma_2(= \sigma)$ as the unique angular coordinate. Thus, the global dynamics can be revealed by the phase portraits (i.e., the level curves of the resonant Hamiltonian in phase space).

The integral of motion Σ_1 can be expressed in terms of the orbital elements as $\Sigma_1 = L\sqrt{(1-e^2)}(1-\cos i) =$ const, which indicates that coupled oscillation occurs between the eccentricity and inclination in the long-term evolution. For convenience, the motion integral Σ_1 can be characterized by the minimum inclination, $I_{\min}$, which corresponds to the inclination when the eccentricity is assumed to be zero; that is, the relation $\Sigma_1 = L(1 - \cos I_{\min})$ holds. For a given $I_{\min}$, the phase portrait in the (σ_2, Σ_2) space can be replaced by the pseudo-phase portrait in the $(e\cos(\sigma_2/2), e\sin(\sigma_2/2))$ space.

In Fig. 6, we take $I_{\min} = 46°$ as an example and present the phase portraits for MEO and GSO satellites. The level curves passing through the coordinate center are

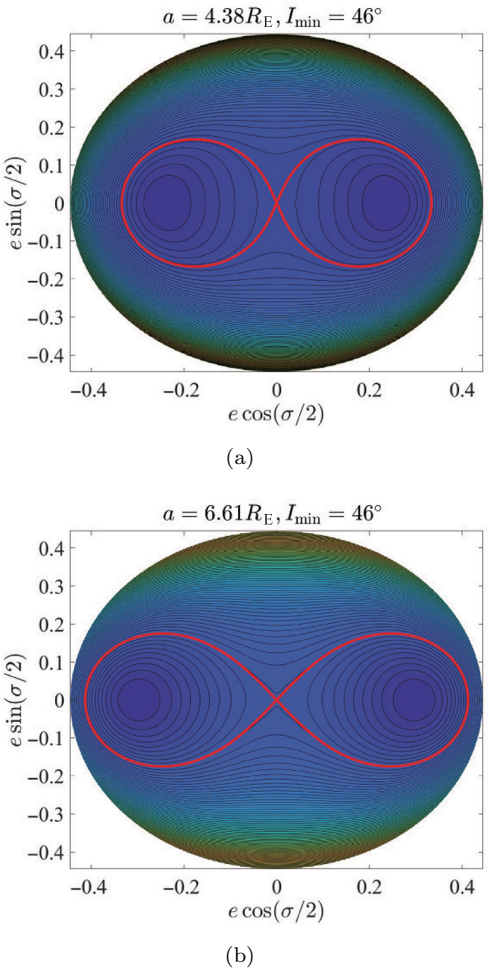

Fig. 6 Phase portraits of the $2g+2h$ resonance ($\sigma = 2g+2h$). Red lines represent the dynamical separatrices (the same as the ones in Figs. 7–11).

shown as red lines. We can observe that (i) the dynamical separatrix stemming from the coordinate center divides the phase space into regions of libration and circulation, (ii) the resonant center is located at $\sigma = 0$, and (iii) the islands of libration are bounded by the separatrices. A comparison of the top and bs reveals that the libration zone for GSO satellites is larger than that for MEO satellites.

3.3.2 $2g + h$ resonance

Similarly, the following linear transformation is introduced to characterize the resonance with $\sigma = 2g + h(= 2\omega + \Omega)$:

$$\begin{cases} \Sigma_1 = G - 2H, & \sigma_1 = g \\ \Sigma_2 = H, & \sigma_2 = 2g + h = \sigma \\ \Sigma_3 = T, & \sigma_3 = \tau \end{cases} \tag{20}$$

It is not difficult to demonstrate that the relation given by Eq. (20) is a canonical transformation with the generating function $\mathcal{S} = g(\Sigma_1 + 2\Sigma_2) + h\Sigma_2 + \tau\Sigma_3$.

Thus, the resonant Hamiltonian can be written as

$$\begin{aligned}\mathcal{H} = & -\frac{1}{16}\mathcal{C}_{J_2}(3\cos 2\alpha+1)\left[\frac{3\Sigma_2^2}{(\Sigma_1+2\Sigma_2)^5}-\frac{1}{(\Sigma_1+2\Sigma_2)^3}\right] \\ & -\frac{1}{32}\mathcal{C}_{\mathrm{SM}}(3\cos^2(\varepsilon-\alpha)-1)\left[\frac{5L^2}{(\Sigma_1+2\Sigma_2)^2}-3\right] \\ & \cdot[3\Sigma_2^2-(\Sigma_1+2\Sigma_2)^2] \\ & +\frac{15}{32}\mathcal{C}_{\mathrm{SM}}\sin 2(\varepsilon-\alpha)\left[L^2\frac{(\Sigma_1+3\Sigma_2)}{(\Sigma_1+2\Sigma_2)^2}-(\Sigma_1+3\Sigma_2)\right] \\ & \cdot\sqrt{\Sigma_1^2+3\Sigma_2^2+4\Sigma_1\Sigma_2}\cos\sigma_2 \end{aligned} \tag{21}$$

The angular coordinates σ_1 and σ_3 are both cyclic; therefore, their conjugate momenta Σ_1 and Σ_3 are the integral of motion. Thus, the dynamical model described by the Hamiltonian of Eq. (21) has one degree of freedom. The global dynamics are revealed by phase portraits characterized by the motion integral Σ_1. Σ_1 can be expressed in terms of the orbital elements as $\Sigma_1 = L\sqrt{1-e^2}(1-2\cos i) = \text{const}$.

This equation shows that the eccentricity and inclination undergo coupled oscillation during the long-term evolution. For a given Σ_1, the inclination takes its maximum value $I_{\max}$ when the eccentricity is assumed to be zero. Thus, there is a one-to-one correspondence between Σ_1 and $I_{\max}$, which indicates that we can use the maximum inclination $I_{\max}$ to represent the motion integral Σ_1. Note that the resonance with $\sigma = 2g+h$ was studied by Ref. [26] in the geocentric equatorial reference frame (please refer to their paper for details).

In practical simulations, we take $I_{\max} = 55.8°$ as an example. The level curves of the resonant Hamiltonian associated with $\sigma = 2g+h$ in the $(e\cos(\sigma/2), e\sin(\sigma/2))$ space are presented in Fig. 7 for MEO and GSO satellites. The level curves passing through the coordinate center are shown in red lines. We can observe that (i) the libration centers are located at $\sigma = 0$, (ii) the dynamical separatrix stemming from the coordinate center divides the phase space into domains of libration and circulation, (iii) the islands of resonance are bounded by the dynamical separatrices, and (iv) GSO satellites have a larger libration zone than MEO satellites.

3.3.3 2g resonance

The resonant Hamiltonian for the secular resonance with

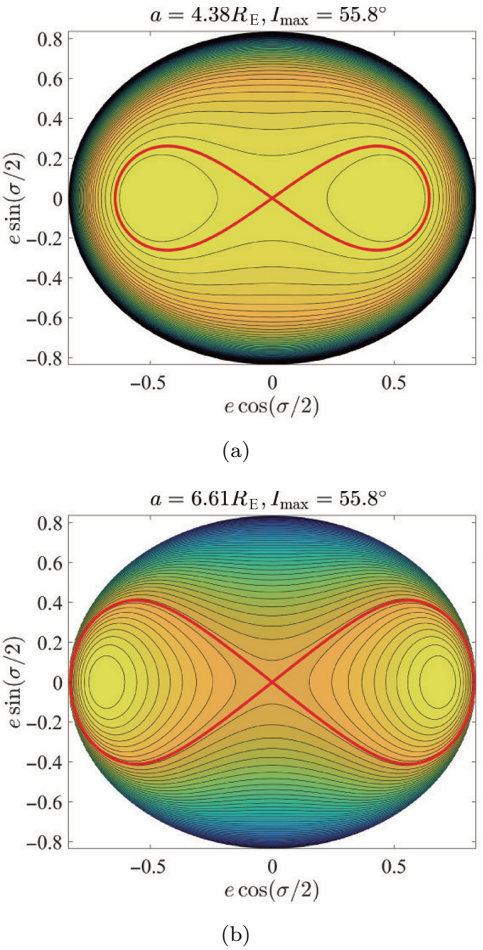

Fig. 7 Phase portraits of the $2g+h$ resonance ($\sigma = 2\omega+\Omega$).

critical argument of $\sigma = 2g$ can be written as

$$\begin{aligned}\mathcal{H} = & -\frac{1}{16}\mathcal{C}_{J_2}(3\cos 2\alpha+1)\frac{1}{G^5}(3H^2-G^2) \\ & -\frac{1}{32}\mathcal{C}_{\mathrm{SM}}(3\cos^2(\varepsilon-\alpha)-1)\left(5L^2\frac{1}{G^2}-3\right) \\ & \cdot(3H^2-G^2) \\ & -\frac{15}{32}\mathcal{C}_{\mathrm{SM}}(3\cos^2(\varepsilon-\alpha)-1)\left(L^2\frac{1}{G^2}-1\right) \\ & \cdot(G^2-H^2)\cos\sigma \end{aligned} \tag{22}$$

which describes a resonant model with one degree of freedom. The action variable H is the integral of motion: $H = L\sqrt{1-e^2}\cos i = \text{const}$.

Similarly, H can be replaced by the maximum inclination $I_{\max}$ (which is the inclination when the eccentricity is taken to be 0). For a given $I_{\max}$, the global dynamics of the resonance can be determined from the corresponding phase portrait.

In practical simulations, we take $I_{\max} = 63°$ as an example. The phase-space structures for MEO and GSO

satellites are shown in Fig. 8, where the level curves passing through the coordinate center are shown as red lines. It is observed that (i) the libration center is located at $\sigma = \pi$, (ii) the separatrix stemming from the coordinate center divides the libration and circulation regions, and (iii) GSO satellites have a larger libration zone than MEO satellites.

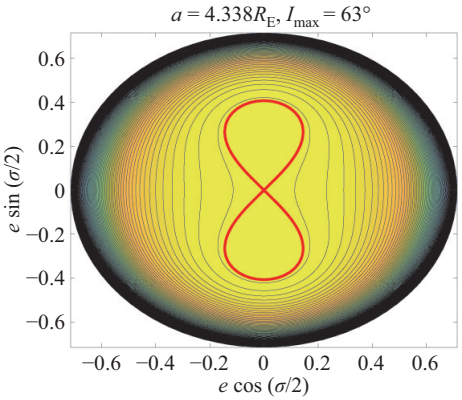

(a)

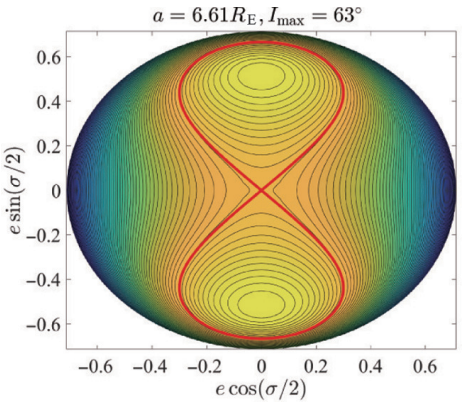

(b)

Fig. 8 Phase portraits of the $2g$ resonance ($\sigma = 2g$).

This resonance with $\sigma = 2\omega$ corresponds to the well-known Kozai resonance [23]. The structures of the phase portraits shown in Fig. 8 are similar to those of the conventional Kozai resonance [27].

3.3.4 $2g - h$ resonance

To study the resonance with $\sigma = 2g - h(= 2\omega - \Omega)$, we introduce the following linear transformation:

$$\begin{cases} \Sigma_1 = G + 2H, & \sigma_1 = g \\ \Sigma_2 = -H, & \sigma_2 = 2g - h = \sigma \\ \Sigma_3 = -T, & \sigma_3 = -\tau \end{cases} \tag{23}$$

which is a canonical transformation with the generating function $\mathcal{S} = g(\Sigma_1 + 2\Sigma_2) - h\Sigma_2 - \tau\Sigma_3$.

For the transformation given by Eq. (23), the resonant Hamiltonian is of the form

$$\begin{aligned} \mathcal{H} = & -\frac{1}{16}\mathcal{C}_{J_2}(3\cos 2\alpha + 1)\frac{1}{(\Sigma_1 + 2\Sigma_2)^5} \\ & \cdot [3\Sigma_2^2 - (\Sigma_1 + 2\Sigma_2)^2] \\ & - \frac{1}{32}\mathcal{C}_{\rm SM}(3\cos^2(\varepsilon - \alpha) - 1)\left[5L^2\frac{1}{(\Sigma_1 + 2\Sigma_2)^2} - 3\right] \\ & \cdot [3\Sigma_2^2 - (\Sigma_1 + 2\Sigma_2)^2] \\ & - \frac{15}{32}\mathcal{C}_{\rm SM}\sin 2(\varepsilon - \alpha)\left[\frac{L^2}{(\Sigma_1 + 2\Sigma_2)^2} - 1\right] \\ & \cdot (\Sigma_1 + 3\Sigma_2)\sqrt{(\Sigma_1 + 2\Sigma_2)^2 - \Sigma_2^2}\cos\sigma_2 \end{aligned} \tag{24}$$

which describes a single-degree-of-freedom system with $\sigma_2(= \sigma)$ as the unique angular coordinate. Because σ_1 and σ_2 do not appear in the resonant Hamiltonian, their conjugate variables Σ_1 and Σ_3 are the integral of motion. The motion integral Σ_1 can be expressed in terms of the orbital elements as $\Sigma_1 = L\sqrt{1 - e^2}(1 + 2\cos i) = \text{const}$.

Consequently, Σ_1 can be replaced by the maximum inclination $I_{\max}$ (the value of the inclination when the eccentricity is taken as zero).

We take $I_{\max} = 69°$ as an example. The phase-space structures of the $2g - h$ resonance for MEO and GSO satellites are shown in Fig. 9, where the level curves passing through the coordinate center are shown as red lines. The structures in the phase portraits for the resonance with $\sigma = 2g - h$ are similar to those for the $2g$ resonance (see Fig. 8).

3.3.5 $2g - 2h$ resonance

To study the resonance with $\sigma = 2g - 2h(= 2\omega - 2\Omega)$, a new set of variables is denoted by $(\Sigma_1, \Sigma_2, \Sigma_3, \sigma_1, \sigma_2, \sigma_3)$. For the generating function given by $\mathcal{S} = g(\Sigma_1 + 2\Sigma_2) - 2h\Sigma_2 - \frac{1}{2}\tau\Sigma_3$, the following canonical transformation is introduced:

$$\begin{cases} \Sigma_1 = G + H, & \sigma_1 = g \\ \Sigma_2 = -\dfrac{1}{2}H, & \sigma_2 = 2g - 2h = \sigma \\ \Sigma_3 = -2T, & \sigma_3 = -\dfrac{1}{2}\tau \end{cases} \tag{25}$$

The resonant Hamiltonian thus has the following form:

$$\begin{aligned} \mathcal{H} = & -\frac{1}{16}\mathcal{C}_{J_2}(3\cos 2\alpha + 1)\left[\frac{12\Sigma_2^2}{(\Sigma_1 + 2\Sigma_2)^5} - \frac{1}{(\Sigma_1 + 2\Sigma_2)^3}\right] \\ & - \frac{1}{32}\mathcal{C}_{\rm SM}(3\cos^2(\varepsilon - \alpha) - 1)\left[\frac{5L^2}{(\Sigma_1 + 2\Sigma_2)^2} - 3\right] \\ & \cdot [12\Sigma_2^2 - (\Sigma_1 + 2\Sigma_2)^2] \end{aligned}$$

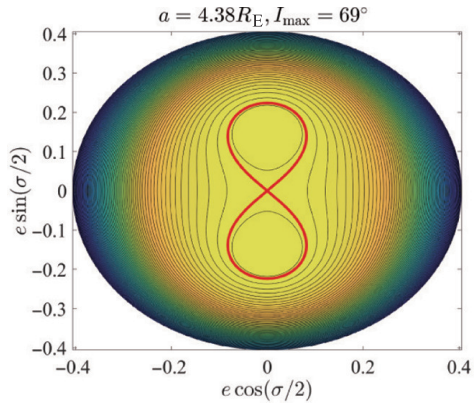

(a)

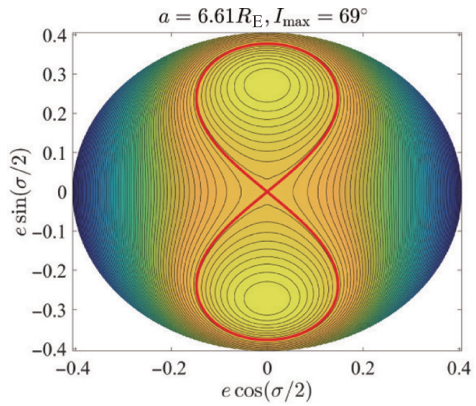

(b)

Fig. 9 Phase portraits of the $2g-h$ resonance ($\sigma = 2\omega-\Omega$).

$$-\frac{15}{64}\mathcal{C}_{\mathrm{SM}}\sin^2(\varepsilon-\alpha)\left[\frac{L^2}{(\Sigma_1+2\Sigma_2)^2}-1\right]\cdot(\Sigma_1+4\Sigma_2)^2\cos\sigma_2 \tag{26}$$

which describes a resonant model with one degree of freedom. The angular coordinates σ_1 and σ_3 are cyclic; thus, their conjugate momenta are the integral of motion. The motion integral Σ_1 can be written in terms of the orbital elements as $\Sigma_1 = L\sqrt{1-e^2}(1+\cos i) = \text{const}$. Consequently, the motion integral Σ_1 can be represented by the maximum inclination $I_{\max}$, which corresponds to the inclination when the eccentricity is zero.

Taking $I_{\max} = 75°$ as an example, we show the phase portraits of the $2g-2h$ resonance in Fig. 10 for MEO and GSO satellites. The figure shows that (i) the saddle points are located at $\sigma = 0$, (ii) the libration center is located at $\sigma = \pi$, and (iii) the dynamical separatrices originating at saddle points (shown as red lines) divide the regions of circulation and libration.

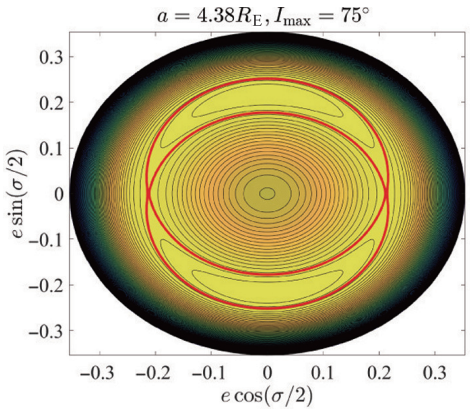

(a)

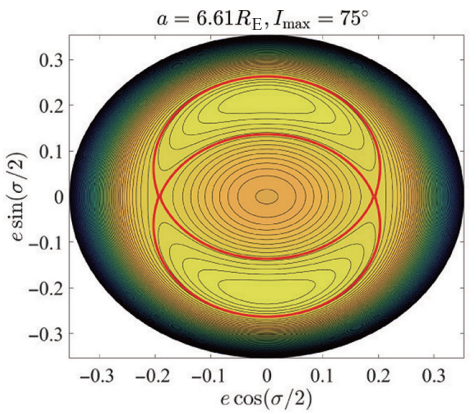

(b)

Fig. 10 Phase portraits of the $2g-2h$ resonance ($\sigma = 2\omega-2\Omega$).

3.4 Lunar node resonances

In this section, the lunar node resonances are discussed. Their critical arguments are given by $\sigma = 2h-\tau(=2\Omega-\Omega_{\mathrm{M}})$ and $\sigma = h-\tau(=\Omega-\Omega_{\mathrm{M}})$. As discussed above, the nodal resonances have dynamical effects only on the variation of the inclination, which changes the orbital planes of satellites.

To study the resonance with $\sigma = 2h-\tau(=2\Omega-\Omega_{\mathrm{M}})$, the following linear transformation is introduced:

$$\begin{cases}\Sigma_1 = G, & \sigma_1 = g\\ \Sigma_2 = \dfrac{1}{2}H, & \sigma_2 = 2h-\tau = \sigma\\ \Sigma_3 = H+2T, & \sigma_3 = \dfrac{1}{2}\tau\end{cases} \tag{27}$$

which is a canonical equation with the generating function $\mathcal{S} = g\Sigma_1 + 2h\Sigma_2 + \tau\left(\frac{1}{2}\Sigma_3 - \Sigma_2\right)$.

Thus, the resonant Hamiltonian can be written as

$$\mathcal{H} = -\dot{\tau}\times\Sigma_2 - \frac{1}{16}\mathcal{C}_{J_2}(3\cos 2\alpha+1)\frac{12\Sigma_2^2}{\Sigma_1^5}$$

$$
\begin{aligned}
&-\frac{1}{32}\mathcal{C}_{\mathrm{SM}}(3\cos^2(\varepsilon-\alpha)-1)\left(5L^2\frac{1}{\Sigma_1^2}-3\right)(12\Sigma_2^2-\Sigma_1^2)\\
&-\frac{3}{64}\mathcal{C}_{\mathrm{M}}\sin(\varepsilon-\alpha)(1+\cos(\varepsilon-\alpha))\sin 2i_{\mathrm{M}}\\
&\cdot\left(5L^2\frac{1}{\Sigma_1^2}-3\right)(\Sigma_1^2-4\Sigma_2^2)\cos\sigma_2 \qquad (28)
\end{aligned}
$$

and defines a resonant model with one degree of freedom. In this model, the actions Σ_1 and Σ_3 are conserved quantities.

As for the resonance with $\sigma = h - \tau(= \Omega - \Omega_{\mathrm{M}})$, the following linear transformation is introduced:

$$
\begin{cases}
\Sigma_1 = G, & \sigma_1 = g\\
\Sigma_2 = H, & \sigma_2 = h-\tau = \sigma\\
\Sigma_3 = H+T, & \sigma_3 = \tau
\end{cases} \qquad (29)
$$

which is canonical and has the generating function $\mathcal{S} = g\Sigma_1 + h\Sigma_2 + \tau(\Sigma_3 - \Sigma_2)$.

When this linear transformation is used, the resonant Hamiltonian becomes

$$
\begin{aligned}
\mathcal{H} &= -\dot{\tau}\times\Sigma_2 - \frac{1}{16}\mathcal{C}_{J_2}(3\cos 2\alpha+1)\frac{3\Sigma_2^2}{\Sigma_1^5}\\
&-\frac{1}{32}\mathcal{C}_{\mathrm{SM}}(3\cos^2(\varepsilon-\alpha)-1)\left(5L^2\frac{1}{\Sigma_1^2}-3\right)(3\Sigma_2^2-\Sigma_1^2)\\
&-\frac{3}{32}\mathcal{C}_{\mathrm{M}}(2\cos(\varepsilon-\alpha)-1)(\cos(\varepsilon-\alpha)+1)\sin 2i_{\mathrm{M}}\\
&\cdot\left(5L^2\frac{\Sigma_2}{\Sigma_1^2}-3\Sigma_2\right)\sqrt{\Sigma_1^2-\Sigma_2^2}\cos\sigma_2\\
&-\frac{3}{128}\mathcal{C}_{\mathrm{M}}(1+\cos(\varepsilon-\alpha))^2\sin^2 i_{\mathrm{M}}\left(5L^2\frac{1}{\Sigma_1^2}-3\right)\\
&\cdot(\Sigma_1^2-\Sigma_2^2)\cos 2\sigma_2 \qquad (30)
\end{aligned}
$$

which describes a single-degree-of-freedom system. The actions Σ_1 and Σ_3 are again conserved quantities.

For both nodal resonances, the action variable $\Sigma_1 = G$ is the integral of motion: $G = L\sqrt{1-e^2} = \text{const}$. Thus, G can be represented by the eccentricity e.

The case of $e = 0.1$ is taken as an example, and the level curves of the resonant Hamiltonian are presented in Fig. 11 for MEO satellites. The dynamical separatrices originating at saddle points are shown as red lines. The libration centers of both resonances, $\sigma = 2h - \tau$ and $\sigma = h - \tau$, are located at $\sigma = \pi$, and their saddle points are located at $\sigma = 0$. Note that these two lunar node resonances were studied by Zhu [5] under the geocentric equatorial reference frame using perturbation theory based on Lie series transformation.

4 Resonance width

The Hamiltonian functions associated with the secular resonances of interest were explicitly presented in the previous section, and their phase portraits were briefly analyzed. The Hamiltonian for a resonance with σ as the resonant angle can generally be written as

$$\mathcal{H} = \mathcal{D}_0 + \mathcal{D}_1\cos\sigma + \mathcal{D}_2\cos 2\sigma \qquad (31)$$

where the coefficients $\mathcal{D}_0$, $\mathcal{D}_1$, and $\mathcal{D}_2$ depend on the action variable Σ, which is conjugate to the resonant angle σ. Note that for all the resonances considered in the preceding section, $\mathcal{D}_2$ is non-zero only for the resonance with $\sigma = h - \tau$.

Using the method presented in Ref. [8], the Hamiltonian can be expanded around the resonant center at $\Sigma = \Sigma^*$ in a Taylor series of $\Delta\Sigma = \Sigma - \Sigma^*$. Neglecting those terms with order higher than 3, we obtain the pendulum-like model governed by

$$\mathcal{H}(\sigma,\Delta\Sigma) = \frac{1}{2}\frac{\partial^2\mathcal{D}_0}{\partial\Sigma^2}\Delta\Sigma^2 + \mathcal{D}_1\cos\sigma + \mathcal{D}_2\cos 2\sigma \qquad (32)$$

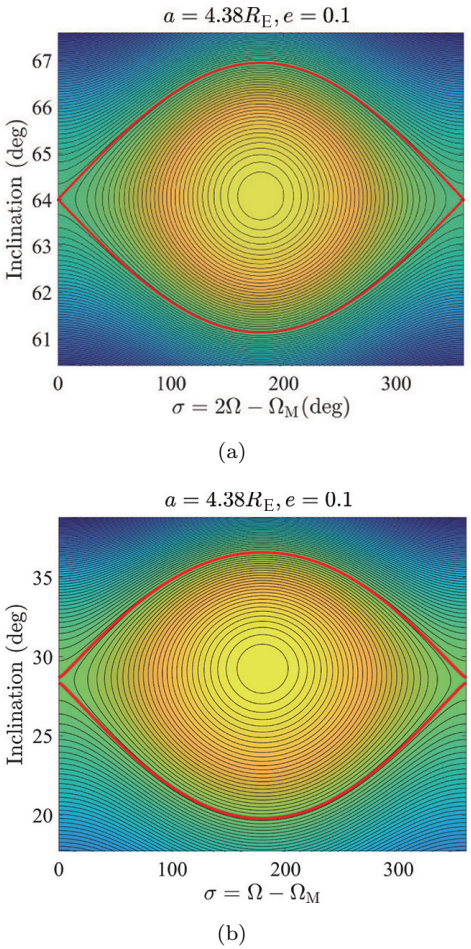

Fig. 11 Phase portraits of the lunar node resonances with critical arguments of $\sigma = 2\Omega - \Omega_{\mathrm{M}}$ (a) and of $\sigma = \Omega - \Omega_{\mathrm{M}}$ (b).

where the terms $\frac{\partial^2 \mathcal{D}_0}{\partial \Sigma^2}$, $\mathcal{D}_1$, and $\mathcal{D}_2$ are evaluated at $\Sigma = \Sigma^*$. According to the resonant model given by Eq. (32), the eigenfrequency at the resonant center (σ^*, Σ^*) is

$$\omega_0 = \sqrt{\frac{\partial^2 \mathcal{D}_0}{\partial \Sigma^2}(\mathcal{D}_1 + 4\mathcal{D}_2)} \tag{33}$$

and thus the timescale of the resonance can be estimated as

$$T = \frac{2\pi}{\omega_0} \tag{34}$$

It is known that the distance between the separatrices stand for the resonant width. Thus, the resonant half-width in terms of $\Delta\Sigma$ is given by

$$\Delta\Sigma = 2\sqrt{\left|\frac{\mathcal{D}_1(\Sigma)}{\frac{\partial^2 \mathcal{D}_0(\Sigma)}{\partial \Sigma^2}}\right|_{\Sigma=\Sigma^*}} \tag{35}$$

Based on the relationship between $\Delta\Sigma$ and the elements e and i (which is different for different resonances), it is not difficult to derive the resonant half-width in terms of the variation of the eccentricity or inclination (Δe or Δi) for each resonance. In practical simulations, the distribution of the resonance width is produced in two cases.

In the first case, the eccentricity is fixed at $e_0 = 0.1$. Figure 12 presents the resonance widths in the (i, a) space for secular resonances occurring at the critical inclinations (a) and for the nodal resonances (b). The corresponding critical arguments are marked in each plot for clarity. In Fig. 12(a), we can observe that (i) the resonance width increases with the semimajor axis, and (ii) among the five resonances occurring at the critical inclinations, the resonance 2ω has the largest width and thus is the strongest.

In the second case, the semimajor axis is assumed to be $a_0 = 4.38R_\mathrm{E}$, which corresponds to the value for MEO satellites in the Beidou Navigation Satellite (BDS) system. Figure 13 shows the resonance widths in the (e, i) space for the secular resonances occurring at the critical inclinations (a) and for lunar node resonances (b). As shown in Fig. 13(a), the resonance width first increases and then decreases as the eccentricity changes from zero to unity. In addition, in high-eccentricity regions the resonance zones of two adjacent resonances may overlap, resulting in chaotic motion [28].

5 Numerical validation

In this section, the equations of motion given by Eq. (6) are numerically integrated with initial elements uniformly

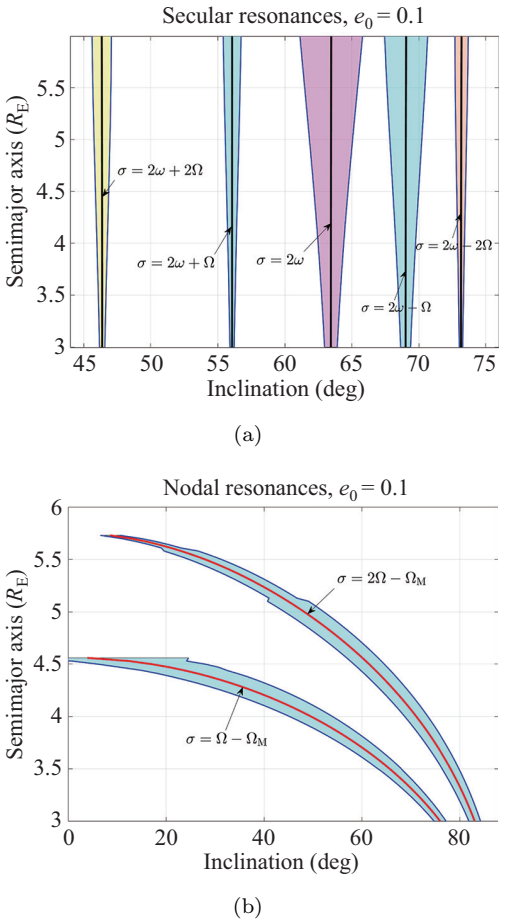

Fig. 12 Resonance widths in the space (a, i) for the secular resonances occurring at the critical inclinations (a) and lunar node resonances (b).

distributed in a certain domain. During the integration period, we record the maximum and minimum values of the eccentricity (e_max and e_min) and inclination (i_max and i_min). To characterize the dynamical effects of secular resonances, we introduce two indicators: (i) the variation of the inclination, denoted by $\Delta i = i_\mathrm{max} - i_\mathrm{min}$, and (ii) the normalized variation of the eccentricity, defined by $\Delta e = \frac{|e_0 - e_\mathrm{max}|}{|e_0 - e_\mathrm{re\text{-}entry}|}$, where e_0 and $e_\mathrm{re\text{-}entry}$ are the initial eccentricity and the eccentricity that leads to re-entry for a given semimajor axis, respectively. $e_\mathrm{re\text{-}entry}$ is calculated by $a_0(1 - e_\mathrm{re\text{-}entry}) = R_\mathrm{E} + 120$ km. The indicator Δe has been widely used in previous studies to produce dynamical maps [10, 29]. However, the indicator Δi is rarely used. In this study, both indicators are used.

According to Eq. (34), the timescale at the resonance center can be estimated. In particular, it is $\sim$730 years for the resonance associated with $\sigma = 2g+2h$, $\sim$846 years for $\sigma = 2g + h$, $\sim$272 years for $\sigma = 2g$, $\sim$328 years for

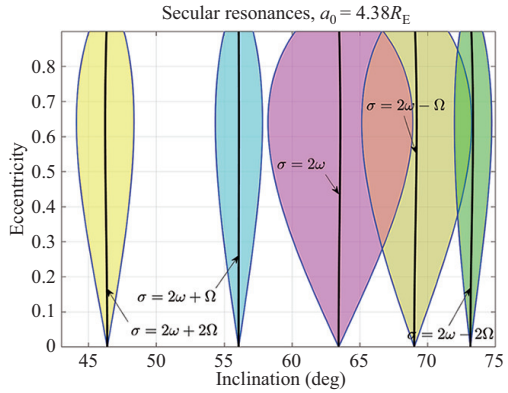

(a)

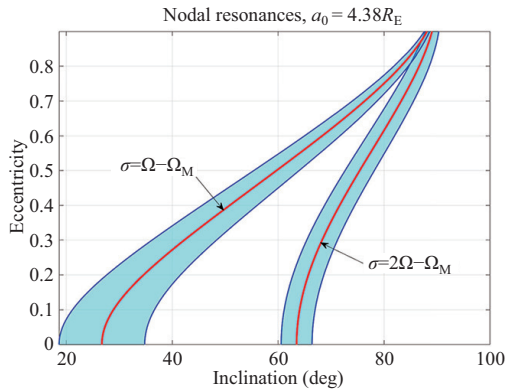

(b)

Fig. 13 Resonance widths in the space (e, i) for the secular resonances occurring at the critical inclinations (a) and lunar node resonances (b).

$\sigma = 2g - h$, and $\sim$846 years for $\sigma = 2g + 2h$ (note that the timescales are evaluated using $a_0 = 3R_E$ and $e_0 = 0.1$ and they may be slightly different for other parameters). In addition, Zhu [5] showed that the timescales of the lunar nodal resonances are shorter than 1000 years (see Figs. 5, 6, and 8 in his paper). Thus, in our simulations, the propagation time is taken as 1000 years, which covers the timescales of the lunisolar resonances considered.

5.1 Dynamical maps at zero eccentricity

When the eccentricity is assumed as zero, the dynamical model given by Eq. (6) reduces to a system with one and half degrees of freedom (the degree of freedom associated with the eccentricity disappears). Thus, the secular resonances occurring at the critical inclinations disappear, and only the nodal resonances exist. For the numerical integration, the initial semimajor axis and inclination are assumed to be distributed in the domain $[3, 6] \times [0°, 90°]$, and the longitude of the ascending node and argument of pericenter are taken as zero. As the eccentricity is always zero, the indicator Δe is not relevant. In this case, we record the variation of the inclination Δi as a function of the initial semimajor axis and inclination. Thus, a dynamical map with Δi as an indicator can be produced.

In Fig. 14(a), we show the field of Δi in degree in the space (i, a), which overlaps the curves of the nodal resonances. For comparison, the resonant widths of the nodal resonances are shown in Fig. 14(b). We can conclude that (i) in the region where nodal resonance occurs, the inclination has a larger variation; (ii) the structure appearing on the dynamical map is in good agreement with the resonance curves, indicating that the nodal resonances form the fundamental structures in the phase space for satellites moving in circular or quasi-circular orbits.

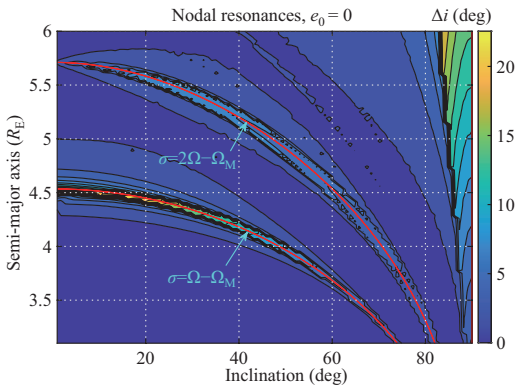

(a)

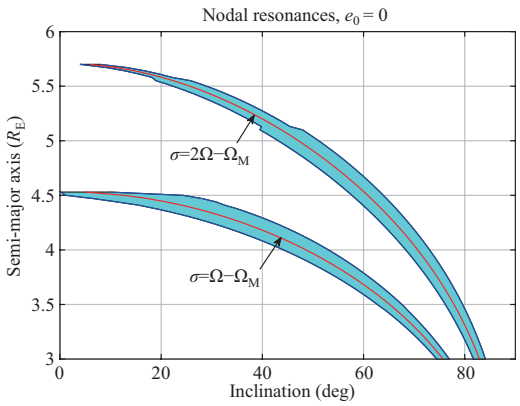

(b)

Fig. 14 Dynamical map with Δi as indicator (a) as well as resonance width of the nodal resonances (b).

5.2 Dynamical maps at non-zero eccentricity

When the eccentricity is different from zero, the

dynamical model represented by Eq. (6) is of two and half degrees of freedom. In the numerical integration, the initial semimajor axis, eccentricity, and inclination are taken in a certain range, and the angle variables, including the longitude of the ascending node and argument of pericenter, are assumed to be zero (simulations showed that dynamical maps remained unchanged when non-zero initial angular variables were used). The indicators Δe and Δi are recorded as functions of the initial semimajor axis, eccentricity, and inclination. For convenience of display, we fix one of the parameters a_0, e_0, and i_0 and present the distribution of Δe or Δi in the space spanned by the other two parameters.

In the practical simulations, the initial eccentricity is fixed at $e_0 = 0.1$. The indicators Δe and Δi are distributed in the space (i_0, a_0), as shown in Fig. 15, where the initial semimajor axis and inclination are uniformly distributed in the domain $[3, 6] \times [0°, 90°]$. The color index represents the magnitude of Δe or Δi.

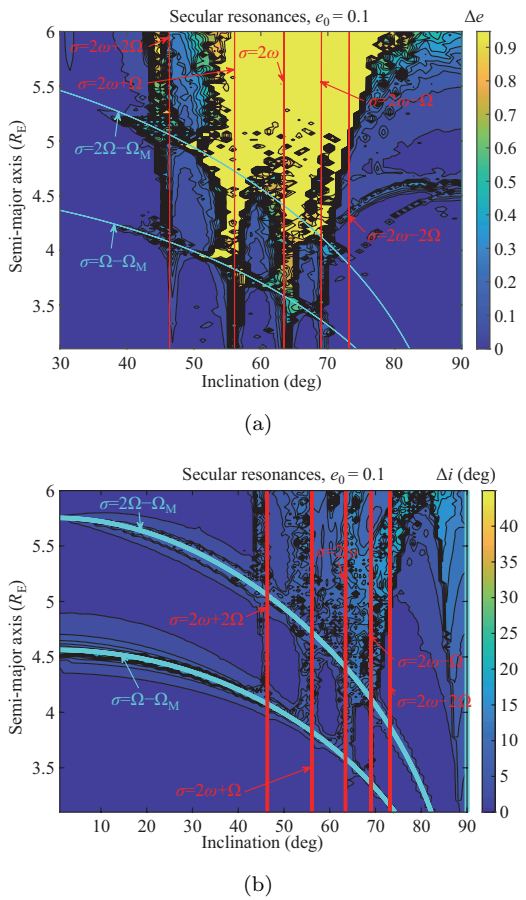

Fig. 15 Dynamical maps with Δe as indicator (a) and with Δi as indicator (b). In each panel, the resonance curves are provided for the purpose of comparison.

For comparison, the resonance curves obtained by the analytical method are plotted in Fig. 15. According to the map of Δe, the secular resonances at the critical inclinations are well identified on the dynamical map, and the structures are slightly distorted around the intersection points of two resonance curves, where chaotic motion occurs. In the field of Δi, both the secular resonances occurring at the critical inclinations and lunar node resonances are well located, and the regions with higher Δi are in excellent agreement with the resonance curves. Our simulations show that Δi is a good dynamical index for characterizing lunisolar secular resonances.

6 Conclusions

In this work, secular resonances of navigation satellites are investigated under the dynamical model formulated under the geocentric Laplace reference frame. Using the double-averaging technique, an explicit expression is derived for the double-averaged disturbing function, in which the leading terms of the Earth's oblateness perturbation and of the lunisolar gravitational perturbations are taken into account.

There are varieties of lunisolar resonances in the MEO and GSO regions. Among these secular resonances, we are interested in the secular resonances with critical arguments of $2\omega + 2\Omega$, $2\omega + \Omega$, 2ω, $2\omega - \Omega$, and $2\omega - 2\Omega$ and the lunar node resonances with critical arguments of $\Omega - \Omega_M$ and $2\Omega - \Omega_M$. The first five resonances are known to occur at the critical inclinations. For each resonance of interest, a linear transformation is made in order to obtain a system with one degree of freedom. The phase portraits for the considered resonances are provided. From the phase portraits, the resonance centers and dynamical separatrices are identified. Then, the resonance widths in terms of the variation of the inclination are produced in the space (i, a) with fixed eccentricity and in the space (i, e) with fixed semimajor axis. For the resonances occurring at the critical inclinations, it is found that (i) when the eccentricity is fixed, the resonance width is an increasing function of the semimajor axis, and (ii) the resonance width first increases and then decreases when the eccentricity changes from zero to unity. In addition, when the eccentricity is higher than a certain value, nearby resonances may overlap, leading to the occurrence of chaotic motion.

To validate the analytical results, dynamical maps are produced. In the production of dynamical maps, two

indicators are used: (i) variation of inclination Δi, and (ii) normalized variation of eccentricity Δe. The structures appearing in the dynamical maps are in good agreement with the resonance curves. In addition, it is observed that the dynamical maps of Δe could locate only the secular resonances occurring at the critical inclinations, whereas the ones of Δi could locate both the secular resonances occurring at the critical inclinations and lunar node resonances well.

Acknowledgements

This work was performed with the financial support of the National Natural Science Foundation of China (No. 12073011).

Declaration of competing interest

The authors have no competing interests to declare that are relevant to the content of this article.

References

[1] Alessi, E. M., Rossi, A., Valsecchi, G. B., Anselmo, L., Pardini, C., Colombo, C., Lewis, H. G., Daquin, J., Deleflie, F., Vasile, M. *et al.* Effectiveness of GNSS disposal strategies. *Acta Astronautica*, **2014**, 99: 292–302.

[2] Allan, R. R., Cook, G. E. The long-period motion of the plane of a distant circular orbit. *Proceedings of the Royal Society of London Series A Mathematical and Physical Sciences*, **1964**, 280(1380): 97–109.

[3] Circi, C., Condoleo, E., Ortore, E. Moon's influence on the plane variation of circular orbits. *Advances in Space Research*, **2016**, 57(1): 153–165.

[4] Ulivieri, C., Circi, C., Ortore, E., Bunkheila, F., Todino, F. Frozen orbital plane solutions for satellites in nearly circular orbit. *Journal of Guidance, Control, and Dynamics*, **2013**, 36(4): 935–945.

[5] Zhu, T. L. On the lunar node resonance of the orbital plane evolution of the Earth's satellite orbits. *Advances in Space Research*, **2018**, 61(11): 2761–2776.

[6] Breiter, S. Lunisolar resonances revisited. In: *Dynamics of Natural and Artificial Celestial Bodies*. Pretka-Ziomek, H., Wnuk, E., Seidelmann, P. K., Richardson, D. L., Eds. Dordrecht: Springer Netherlands, **2001**: 81–91.

[7] Rosengren, A. J., Alessi, E. M., Rossi, A., Valsecchi, G. B. Chaos in navigation satellite orbits caused by the perturbed motion of the Moon. *Monthly Notices of the Royal Astronomical Society*, **2015**, 449(4): 3522–3526.

[8] Daquin, J., Rosengren, A. J., Alessi, E. M., Deleflie, F., Valsecchi, G. B., Rossi, A. The dynamical structure of the MEO region: Long-term stability, chaos, and transport. *Celestial Mechanics and Dynamical Astronomy*, **2016**, 124(4): 335–366.

[9] Todorović, N., Novaković, B. Testing the FLI in the region of the Pallas asteroid family. *Monthly Notices of the Royal Astronomical Society*, **2015**, 451(2): 1637–1648.

[10] Gkolias, I., Daquin, J., Gachet, F., Rosengren, A. J. From order to chaos in Earth satellite orbits. *The Astronomical Journal*, **2016**, 152(5): 119.

[11] Rosengren, A. J., Daquin, J., Tsiganis, K., Alessi, E. M., Deleflie, F., Rossi, A., Valsecchi, G. B. Galileo disposal strategy: Stability, chaos and predictability. *Monthly Notices of the Royal Astronomical Society*, **2017**, 464(4): 4063–4076.

[12] Sanchez, D. M., Yokoyama, T., de Almeida Prado, A. F. B. Study of some strategies for disposal of the GNSS satellites. *Mathematical Problems in Engineering*, **2015**, 2015: 1–14.

[13] Tang, J. S., Hou, X. Y., Liu, L. Long-term evolution of the inclined geosynchronous orbit in Beidou Navigation Satellite System. *Advances in Space Research*, **2017**, 59(3): 762–774.

[14] Lei, H. L. Dynamical models for secular evolution of navigation satellites. *Astrodynamics*, **2020**, 4(1): 57–73.

[15] Yokoyama, T. Dynamics of some fictitious satellites of Venus and Mars. *Planetary and Space Science*, **1999**, 47(5): 619–627.

[16] Lane, M. T. On analytic modeling of lunar perturbations of artificial satellites of the earth. *Celestial Mechanics and Dynamical Astronomy*, **1989**, 46(4): 287–305.

[17] Lei, H. L., Circi, C., Ortore, E. Modified double-averaged Hamiltonian in hierarchical triple systems. *Monthly Notices of the Royal Astronomical Society*, **2018**, 481(4): 4602–4620.

[18] Cook, G. E. Luni-solar perturbations of the orbit of an earth satellite. *Geophysical Journal of the Royal Astronomical Society*, **1962**, 6(3): 271–291.

[19] Hughes, S. Earth satellite orbits with resonant lunisolar perturbations I. Resonances dependent only on inclination. *Proceedings of the Royal Society of London A Mathematical and Physical Sciences*, **1980**, 372(1749): 243–264.

[20] Zhao, C. Y., Zhang, M. J., Wang, H. B., Xiong, J. N., Zhu, T. L., Zhang, W. Analysis on the long-term dynamical evolution of the inclined geosynchronous orbits in the Chinese BeiDou navigation system. *Advances in Space Research*, **2015**, 56(3): 377–387.

[21] Ely, T. A., Howell, K. C. Dynamics of artificial satellite orbits with tesseral resonances including the effects of luni-solar perturbations. *Dynamics and Stability of Systems*, **1997**, 12(4): 243–269.

[22] Brouwer, D. Solution of the problem of artificial satellite theory without drag. *The Astronomical Journal*, **1959**, 64: 378.
[23] Kozai, Y. Secular perturbations of asteroids with high inclination and eccentricity. *The Astronomical Journal*, **1962**, 67: 591.
[24] Deprit, A. Canonical transformations depending on a small parameter. *Celestial Mechanics*, **1969**, 1(1): 12–30.
[25] Hori, G. Theory of general perturbation with unspecified canonical variable. *Publication of the Astronomical Society of Japan*, **1966**, 18(4): 287.
[26] Celletti, A., Galeş, C. B. A study of the lunisolar secular resonance $2\dot{\omega}+\dot{\Omega}=0$. *Frontiers in Astronomy and Space Sciences*, **2016**, 3: 11.
[27] Naoz, S. The eccentric kozai-lidov effect and its applications. *Annual Review of Astronomy and Astrophysics*, **2016**, 54(1): 441–489.
[28] Chirikov, B. V. A universal instability of many-dimensional oscillator systems. *Physics Reports*, **1979**, 52(5): 263–379.
[29] Gkolias, I., Colombo, C. Towards a sustainable exploitation of the geosynchronous orbital region. *Celestial Mechanics and Dynamical Astronomy*, **2019**, 131(4): 1–30.

Hanlun Lei received his Ph.D. degree in astronomy from Nanjing University, China, in 2015. Currently, he is an associate professor at the School of Astronomy and Space Science in Nanjing University. His research interest focuses on astrodynamics and celestial mechanics, including space manifold dynamics in multi-body environments as well as resonance dynamics of minor bodies. E-mail: leihl@nju.edu.cn.

Emiliano Ortore graduated in aerospace engineering (M.S. degree) and astronautical engineering (M.S. degree) and pursued his Ph.D. degree in aerospace engineering at Sapienza University of Rome. Since 2004, he has been working as a researcher at Sapienza University of Rome. His research fields are celestial mechanics, orbits and satellite constellations for Earth observation, telecommunication and navigation, orbits for the observation of planets, moons, and asteroids, and remote sensing applications. E-mail: emiliano.ortore@ uniroma1.it.

Christian Circi is currently an associate professor in flight mechanics at the Department of Astronautical, Electrical and Energy Engineering, Sapienza University of Rome. He received his M.S. degrees in aeronautical engineering and aerospace engineering, and pursued his Ph.D. degree in aerospace engineering at Sapienza University of Rome. He worked as a researcher at the Grupo de Mecanica of Vuelo-Madrid (GMV), and a research assistant at the Department of Aerospace Engineering. He lecturers "interplanetary trajectories" and "flight mechanics of launcher" in the master degree course of space and astronautical engineering at Sapienza University of Rome. His principal research fields are as follows: third-body and solar perturbations, interplanetary and lunar trajectories, solar sail, orbits for planetary observation, and ascent trajectory of Launcher. He is an associate editor for the journals of *Aerospace Science and Technology* and *the International Journal of Aerospace Engineering*. E-mail: christian.circi@uniroma1.it.